

# Identification of competing ultrafast all-optical switching mechanisms in Si woodpile photonic crystals

Philip J. Harding<sup>1,2</sup>, Tijmen G. Euser<sup>1,3</sup>, and Willem L. Vos<sup>1,2</sup>

<sup>1</sup>*Center for Nanophotonics, FOM Institute for Atomic and Molecular Physics (AMOLF),  
Kruislaan 407, 1098 SJ Amsterdam, The Netherlands*

<sup>2</sup>*Complex Photonic Systems (COPS), MESA+ Institute for Nanotechnology, University of  
Twente, 7500 AE Enschede, The Netherlands*

<sup>3</sup>*Currently with Max-Planck Research Group (IOIP), University of Erlangen-Nuremberg,  
Günther-Scharowsky-Str. 1/Bau 24, 91058 Erlangen, Germany*

We present a systematic study of ultrafast all-optical switching of Si photonic band gap woodpile crystals using broadband tunable nondegenerate pump-probe spectroscopy. At pump-probe coincidence, we investigate the behavior the differential reflectivity at the blue edge of the stopband for a wide range of pump- and probe frequencies. Both dispersive and absorptive features are observed from the probe spectra at coincidence. As the pump frequency is tuned through half the electronic bandgap of Si, the magnitude of both these features increases. For the first time we unambiguously identify this dispersive effect with the electronic Kerr effect in photonic crystals, and attribute the the absorptive features to nondegenerate two photon absorption. The dispersive and absorptive nonlinear coefficients are extracted, and are found to agree well with literature. Finally, we propose a nondegenerate figure of merit (NFOM), which defines the quality of switching for all nondegenerate optical switching processes. © 2018 Optical Society of America

*OCIS codes:* 050.5298, 190.3270, 190.4180, 320.7110, 320.2250

## 1. Introduction

The interest to optically switch photonic structures has recently gathered momentum due to the inherent fastness of the process. While the switching speed of conventional transistors is ultimately limited by heat dissipation, no such limitation exists for optical systems in the absence of absorption. To date, the dispersion of photo-induced free carriers is widely exploited to induce ultrafast changes in the photonic structure's optical properties. Then, propagation switching, optical modulation, trapping and releasing photons, frequency- and bandwidth conversion, and even ultrafast switching of the density of states are possible [1–6].

In the past, several groups have switched Si photonic crystals via free carrier excitation [7–9]. This switching mechanism is popular because of its large attainable change in refractive index and its high possible repetition rate. Indeed, currently many efforts are devoted to decreasing the timescales of switching in polycrystalline silicon (p-Si), achievable through implanting additional recombination centers such as ions [10–12]. However, the possible recombination time is still limited to several ps.

Electronic Kerr switching offers the potential to switch instantaneously, with a repetition rate limited only by the duration of the pump pulse. The duration of the pump and probe pulses then controls the repetition rates, instead of the recombination times of the free carriers. Kerr switching could potentially increase the repetition rate from GHz to THz. Unfortunately, the intensities required are typically much higher compared to free carrier switching [13–15]. Recently, several groups have claimed to have experimental evidence of this Kerr nonlinearity in photonic crystals [16–20]. The reasoning in all cases is the instantaneous nature of the effect, resulting in a decrease in reflectivity or transmission at one probe frequency which coincides with the cross-correlation of the pump and probe pulses. Here, we critically evaluate these optical processes at instantaneous (fs) timescales. At pump-probe coincidence, we will show that two competing processes change the optical properties as witnessed from reflectivity measurements performed over a large bandwidth. From these two processes, we propose a general nondegenerate figure of merit (NFOM), which has wide

implications for all-optical fs switching, ultimately extending to DOS switching and the dynamic control of spontaneous emission.

## 2. Experimental setup and sample

Our setup consists of a regeneratively amplified pulsed Ti:Sapph laser (Spectra Physics Hurricane) which drives two independently tunable optical parametric amplifiers (OPAs, Topas). The OPAs have a continuously tunable output frequency between 0.44 and 2.4 eV, with nearly bandwidth limited pulses (relative width of 1.33%, bandwidth limited equivalent to  $\tau_P = 110$  fs) with pulse durations of  $\tau_P = 140 \pm 10$  fs (measured at  $E_{\text{Pump}} = 0.95$  eV) and a pulse energy of at least 20  $\mu\text{J}$ . The probe beam is normally incident  $\theta = 0^\circ$  on the sample, and is focused to a Gaussian spot of 32  $\mu\text{m}$  FWHM (at  $E_{\text{probe}} = 1.24$  eV) at a small angular divergence  $\text{NA} = 0.02$ . The probe intensity  $I_{\text{Probe}}$  of  $3 \pm 2$   $\text{GWcm}^{-2}$  was around 10 times lower than the pump intensity  $I_{\text{Pump}}$  to ensure that nonlinear effects caused by the probe were negligible. The reflectivity was calibrated by referencing to a gold mirror. A versatile measurement scheme was developed to subtract the pump background from the probe signal, and to compensate for possible pulse-to-pulse variations in the output of our laser [21, 22].

Figure 1 shows a high resolution scanning electron micrograph of the photonic woodpile structure made by Jim Fleming at Sandia National Laboratories [23]. It consists of 5 layers of p-Si rods ( $n' = 3.45$ ) stacked orthogonally upon one another, the  $n$ -th layer shifted by half an interrod distance with respect to the  $(n+2)$ th layer, with a total thickness of  $L = 780$  nm. This structure gives rise to a diamond lattice, for which a first-order band gap is predicted [24]. The dimensions of the rods were chosen so as to aim the center of the band gap around telecom frequencies ( $E_{\text{Tele}} = 0.735$  eV). The electric field of the probe beam is polarized along the  $[\bar{1}10]$  direction of the crystal, that is, perpendicular to the first row of rods. The last row of rods is supported by a 70 nm thick SiN layer of refractive index 2.

The sample has been characterized extensively elsewhere [22]. Over the sample, the mutual alignment of the rods differs. These differences are spatially separated, and allow the sample

to be divided into 16 domains, which we denote by A1 through D4 in analogy to a chessboard. Here, we perform measurements on both A1 and D4, and are thus able to validate our results for different sample conditions. The symmetry of D4 is face centered orthorhombic, while A1 is body centered orthorhombic.

### 3. Linear reflectivity

Figure 2 shows a linear reflectivity spectrum of the woodpile photonic crystal. The high peak centered at  $E_0 = 0.9$  eV corresponds to the  $\Gamma - X$  stop gap in the band structure, which is part of the 3D photonic band gap of Si woodpile photonic crystals [21, 25, 26]. The maximum reflectivity of  $95 \pm 2\%$  and the broad width of  $\Delta E = 0.46$  eV FWHM (full width at half maximum) confirm the strong interaction of the crystal with light. The interaction strength  $S$  is characterized by the relative gap width  $S = \Delta E/E_0$  [27]. We note that the large photonic strength of  $S = 47\%$  is the largest measured for any photonic crystal so far.

We can associate a length scale with the photonic strength. The Bragg length  $L_B$  is the length at which the incoming intensity has dropped to  $1/e$  of its initial value, and is given by [28]

$$L_B = \frac{\lambda}{\pi S}, \quad (1)$$

where  $\lambda$  is the wavelength in the structure of the stopgap. We deduce a Bragg length of  $L_B = 840$  nm, corresponding to 1.06 unit cells. In contrast, other 3D structures with a lower photonic strength have a much higher  $L_B$ : For example,  $\text{TiO}_2$  inverse opals have  $L_B \approx 3.3 \mu\text{m}$ , polystyrene opals have  $L_B \approx 5.1 \mu\text{m}$  and  $\text{SiO}_2$  opals  $L_B \approx 6 \mu\text{m}$  [28].

The high quality of the sample also causes the steep edges of the peak, which we will in first instance probe at the blue edge of the stopband. At these frequencies, all induced changes in optical properties of the Si backbone will cause a large change in reflectivity, important for switching applications. The probe frequencies (indicated by the shaded box) span both the blue edge of the stopband as well as the fringes. These have been tentatively assigned to Fabry-Pérot-type interferences [29], but the interpretation of the reflectivity spectrum of

woodpiles is still an open question [22].

#### 4. Switched reflectivity vs. time at one probe frequency

The pump frequencies  $E_{\text{Pump}}$  were chosen as to tune through half the electronic band gap of silicon, where the gap is  $E_G = 1.12$  eV. Both the Kerr coefficient  $n_2$  and the degenerate two-photon absorption coefficient  $\beta_{11}$  have recently been shown to vary strongly in the vicinity of  $\frac{1}{2}E_G$  [13–15, 30–32]. On domain A1 we measured differential reflectivity  $\Delta R/R$  vs. probe delay  $\Delta t$  as a function of  $E_{\text{Pump}}$  (figure 3). On this domain, the probe frequency  $E_{\text{Probe}} = 1.13$  eV corresponds to the foot of the blue stopband edge. At positive probe delays  $\Delta t = 1$  ps and at pump frequencies  $E_{\text{Pump}} > \frac{1}{2}E_G = 0.56$  eV, we observe a large positive differential reflectivity  $(\Delta R/R)_{\text{FC}}$  due to a blueshift of the photonic features. This shift is caused by a decrease of the refractive index of the p-Si backbone that agrees well with a Drude description of the excited free carriers [21]. When  $E_{\text{Pump}}$  is reduced to below  $\frac{1}{2}E_G$ , the dispersion vanishes, since no free carriers are excited by a two-photon process.

At pump-probe coincidence, near  $\Delta t = 0$  ps, we observe a trough of magnitude  $(\Delta R/R)_{\text{coinc}}$ . The width of this trough varies between 240 fs ( $E_{\text{Pump}} = 0.52$  eV) and 160 fs ( $E_{\text{Pump}} = 0.62$  eV). These widths agree reasonably well with the expected cross-correlation duration for two pulses ( $\tau_P \times \sqrt{2} = 200$  fs). As  $E_{\text{Pump}}$  increases to above  $\frac{1}{2}E_G$ , the magnitude of the instantaneous feature  $(\Delta R/R)_{\text{coinc}}$  grows until it saturates at  $E_{\text{Pump}} = 0.62$  eV, just over  $\frac{1}{2}E_G$ . In all cases, instantaneous switching features are observed.

#### 5. Switched reflectivity vs. frequency

##### 5.A. Reflectivity vs. frequency at coincidence

In order to investigate the precise nature of  $(\Delta R/R)_{\text{coinc}}$ , we have measured the differential reflectivity at coincidence on domain D4 for a wide range of probe frequencies, which we plot in figure 4(c). We make three important observations. Firstly, with increasing  $E_{\text{Pump}}$ , the variation in the data becomes stronger. Secondly, the differential reflectivity becomes

increasingly negative with both increasing pump and increasing probe frequency. These negative values indicate optical absorption. Thirdly, at 1.22 eV, a peak appears in the differential reflectivity that corresponds to a red edge in the linear reflectivity (figure 4(a)); likewise, a trough appears at 1.18 eV which corresponds to a blue edge. This clear dispersive behavior is indicative of a redshift of the photonic features related to a positive change in  $n'$ . Thus we conclude that when pump and probe are coincident, two effects contribute to the differential reflectivity: Nonlinear dispersion, which we attribute to the electronic Kerr effect, and absorption. We conclude that the negative differential reflectivity is due to an instantaneous nondegenerate two photon process, since this absorption is seen to increase for an increase of either pump or probe frequencies, and since the sum of pump and probe frequencies exceeds the absorption edge of p-Si. Recent work [16–20] has attributed the behavior at coincidence to the Kerr effect exclusively, even though dispersive data are lacking. Here, for the first time we identify the different instantaneous contributions to all-optical photonic switching. Therefore, this also represents the first identification of Kerr switching in photonic crystals.

### 5.B. *Reflectivity vs. frequency at $\Delta t = 1$ ps*

Before quantifying the two different instantaneous contributions from the data, we will first briefly describe the measured effects of the free carriers on the spectral properties. Figure 4(b) shows the differential reflectivity at a positive probe delay of  $\Delta t = 1$  ps that is caused by free carriers. Because the differential reflectivity varies around 0, we conclude that the induced absorption is minimal. The peak at 1.2 eV corresponds to the blue edge of the linear reflectivity peak at 1.175 eV, the two troughs at 1.23 eV and 1.16 eV corresponds to the red edges of the reflectivity peaks at 1.175 and 1.25 eV, respectively. Therefore, the data are consistent with a blueshift, or a decrease of the refractive index  $\Delta n'$  as a result of the free carriers.

### 5.C. Model: The Extended Scalar Wave Approximation

To quantify the two nonlinear contributions at coincidence as well as the free carrier effects, a model of the woodpile's linear and nonlinear spectral properties is necessary. To predict the change in complex refractive index, we require a physical model which is subject to two requirements: First, this model must reproduce the linear reflectivity  $R_0$  over a given frequency range. This requirement is necessary because the measured differential reflectivity, defined as  $\frac{\Delta R(t)}{R} \equiv \frac{R(t)-R_0}{R_0}$ , depends sensitively on  $R_0$ . Second, the calculated spectral properties must scale correctly with the induced complex  $n$ .

Here, we employ a heuristic model to calculate both the linear as well as the dynamic reflectivity, which is an extension of the scalar wave approximation (SWA) [33]. The dielectric function in beam direction  $\epsilon(z)$  and the lattice spacing can be written in terms of their Fourier components  $U_G$  and  $G$ , respectively. For binary structures composed of two different dielectric materials, it can be shown that [28]

$$U_G = \Delta\epsilon f_G, G \neq 0, \quad (2)$$

where  $\Delta\epsilon$  is the difference of the dielectric constants, and  $f_G$  is the Fourier Transform of the indicator function  $f(z)$ , where  $\epsilon(z) = \epsilon_1 + \Delta\epsilon f(z)$ . From a change in  $\Delta\epsilon$ , a new  $U_G$  can readily be obtained. The electric field inside the crystal can now be calculated by considering only the first two bands,  $k$  (incident) and  $k - G$  (Bragg diffracted). Outside the crystal, the field can be determined from the two boundary conditions the two bands are subject to. Thus, the transmission and reflectivity can be determined. Recently, Euser *et al.* employed an exact modal method (EMM) to calculate the broadband reflectivity of the woodpile photonic crystal [25]. Although the agreement was good for low frequencies, the reflectivity could not be reproduced faithfully beyond the stopgap [21]. To obtain a better agreement, the number of plane waves would have had to have been increased, for which the calculation diverges slower. Also, Deubel *et al.* achieved good agreement at the blue edge with a scattering matrix

model, although some salient features were still lacking [34]. We verified that at the relevant probe frequencies, the induced shift obtained with SWA matches the EMM (see appendix A).

We fit the linear reflectivity obtained by the scalar wave approximation to the region given in fig. 4(a). The best agreement to the measured reflectivity is obtained with  $G = 2\pi/(393 \text{ nm})$  and  $U_G = -0.8$ . The calculated spectral feature shown corresponds to the first two Fabry-Pérot fringes at the blue edge of the stopgap. In the model, we included the dispersion and absorption of p-Si (from [35], see fig. 5), and have taken bulk Si as the substrate. We verified that the thin layer of SiN ( $n' = 2, d = 70\text{nm}$ ) had no effect on our analysis (appendix B). Since the optical features in the reflectivity spectrum are much broader than the probe bandwidth, no convolution of the calculated spectrum with the probe is necessary.

#### 5.D. Interpretation of spectra at coincidence

We match the calculated dispersive differential reflectivity to the strong signature of a redshift at  $E_{\text{Probe}} = 1.2 \text{ eV}$  by fitting two independent parameters  $\Delta n' = 2n_2 I_{\text{Pump}}$  and  $n'' = \lambda_0 \beta_{12} I_{\text{Pump}} / 2\pi$  over the range  $1.18 \text{ eV} < E_{\text{Probe}} < 1.23 \text{ eV}$  by minimizing the least squares. Here,  $\beta_{12}$  is the nondegenerate two-photon absorption coefficient and  $\lambda_0$  the free space wavelength. The differential reflectivity was obtained as follows: using the  $G$  obtained previously from the fit to the linear spectrum, the  $U_G$  was changed via the changed  $\Delta\epsilon$  (equation 2), and the switched reflectivity spectrum was calculated from the new  $U_G$ . Error margins for the parameters were taken as the values at which the least squares values had changed by 10%.

Figure 4(c) shows the fits to two spectra obtained at two different  $E_{\text{Pump}}$ . The remarkable agreement of this approximate model with the data confirms that the subtle interplay of nonlinear dispersion as well as nondegenerate absorption leads to the observed features. At frequencies below 1.2 eV, the fitted curves tend to be lower than the measurements. Above 1.2 eV, the calculated differential reflectivity is mostly higher than the measurements. These



deviations are due to our fit not taking into account the frequency dependence of  $\beta_{12}$ , but setting it to one value for all probe frequencies.

Figure 5(a) and (b) shows the absorptive and dispersive part of the induced refractive index at coincidence, respectively, as returned from the fits. The value at  $E_{\text{Pump}} = 0.59$  eV is excluded due to an experimental artifact in that measurement. Figure 5(a) shows that the imaginary refractive index  $n''$  increases for pump frequencies  $E_{\text{Pump}} > 0.55$  eV. These frequencies correspond to a sum of pump and probe frequencies  $E_{\text{Pump}} + E_{\text{Probe}} > 1.75$  eV. Since these values are larger than the optical gap of p-Si ( $1.4 \text{ eV} < E_{\text{opt}} < 1.6 \text{ eV}$ , depending on the degree of polycrystallinity [36]), it is clear that the simultaneous presence of pump and probe photons induces optical absorption. The resulting values of the nondegenerate two photon absorption coefficient are  $\beta_{12} = 0.11 \text{ cmGW}^{-1}$  at  $E_{\text{Pump}} = 0.54$  eV and  $\beta_{12} = 0.19 \text{ cmGW}^{-1}$  at  $E_{\text{Pump}} = 0.62$  eV.

From recent calculations [37], the  $N_{\text{ph}}$ -photon process in a direct transition can be viewed as a single-photon process with an energy gap rescaled to  $E_G/N_{\text{ph}}$ , where  $N_{\text{ph}}$  is the number of photons. In other words,  $(E_{\text{Pump}} + E_{\text{Probe}})/2 = E'$  in the present two beam case, where  $E'$  is a rescaled energy. Therefore, we can compare the spectral *shape* of our extracted nondegenerate absorption coefficient to the linear absorption. We therefore also plot the linear absorption of p-Si [35], similar to our woodpile crystals [23]. The behavior of the linear absorption agrees reasonably with that of the nondegenerate absorption, supporting calculations from [37]. For our intensities, the nondegenerate absorption remains significantly below the linear absorption. Pumping or probing at higher frequencies causes the absorption to increase, as do higher pump intensities, but not higher probe intensities [38].

The instantaneous change of the real part of the refractive index  $\Delta n'$  is plotted in figure 5(b). Again the value at  $E_{\text{Pump}} = 0.59$  eV is excluded from the discussion. At low pump frequencies of 0.52 eV, the change is  $0.44 \times 10^{-3}$ , and it more than doubles to  $1.1 \times 10^{-3}$  at  $E_{\text{Pump}} = 0.56$  eV. At  $E_{\text{Pump}} = 0.62$  eV,  $\Delta n'$  decreases slightly. The resulting values of the Kerr coefficients are  $n_2 = 7.3 \times 10^{-6} \text{ cm}^2\text{GW}^{-1}$  at  $E_{\text{Pump}} = 0.54$  eV and  $n_2 = 12.7 \times 10^{-6}$

$\text{cm}^2\text{GW}^{-1}$  at  $E_{\text{Pump}} = 0.62 \text{ eV}$ . We compare our measurements to recent measurements of the degenerate nonlinear dispersion of bulk Si [13–15]. In order to be able to make the comparison, we made use of the rescaling condition. We find excellent agreement to the data from [13, 15], but surprisingly the measurements of [14] are an order of magnitude higher, despite all being measured with the same z-scan technique. We also compare our measured data to a relation for  $n_2$  derived for direct-gap semiconductors [39] multiplied by our pump intensity  $I_{\text{Pump}}$ . The functional form agrees well with our data. At higher probe frequencies, the theoretical relation differs from the data of Refs. [13, 15]. The agreement can be improved by employing a theory for the degenerate nonlinear properties of an indirect semiconductor [37] using the rescaling condition [14].

Having identified the two contributions at pump-probe coincidence, we briefly discuss recent photonic crystal switching experiments in the light of our new interpretation. Becker *et al.* performed time-resolved non-degenerate pump-probe spectroscopy on a-Si and p-Si inverse opals [8]. In their data on the a-Si sample, sharp features indicative of instantaneous absorption are apparent for  $E_{\text{Pump}} = 0.674 \text{ eV}$  and  $E_{\text{Probe}} > 0.653 \text{ eV}$ , or  $E_{\text{Total}} > 1.327 \text{ eV}$  at pump-probe coincidence. Their p-Si sample reveals these sharp features at  $E_{\text{Pump}} = 0.717 \text{ eV}$  and  $E_{\text{Probe}} > 0.539 \text{ eV}$  ( $E_{\text{Total}} > 1.256 \text{ eV}$ ). Because of the lower optical gap  $E_{\text{Opt}}$  for p-Si with respect to a-Si, we expect nondegenerate absorption to take place at a lower  $E_{\text{Total}}$  than for the a-Si sample, in agreement with their data. As a second example, we discuss the contribution by Haché and Bourgeois [16]. Here, the authors probe a Si/SiO<sub>2</sub> Bragg stack at the red edge of the stopgap. At coincidence, they observe a significant increase in transmission. The observed feature can only be explained by the breakdown of destructive interference due to nondegenerate absorption for  $E_{\text{Pump}} = 0.725 \text{ eV}$  and  $E_{\text{Probe}} = 0.821 \text{ eV}$ , giving  $E_{\text{Total}} = 1.546 \text{ eV}$ , comparable to  $E_{\text{Opt}}$  of a-Si. The Kerr effect without induced absorption would lead to a red shift of the stopgap and thus to a decrease in transmission. In a similar manner, the contributions by Mazurenko *et al.*, Hastings *et al.*, and Mondia *et al.* misinterpret the sharp trough in differential reflectivity as the Kerr effect [17–19].

### 5.E. Interpretation of ps switching

Using the same extended SWA from section 5.C, we can also interpret the picosecond free carrier behavior. Therefore, the calculated differential reflectivity can be fitted to  $(\Delta R/R)_{\text{FC}}$  by calculating the complex refractive index change with the Drude model (figure 4(b)). The carrier density  $N$  is given by

$$N = \frac{I_{\text{Pump}}^2 \tau_P \beta_{11}}{2E_{\text{Pump}} e}, \quad (3)$$

where  $\beta_{11}$  is the degenerate two photon absorption coefficient. At our pump frequencies, we can neglect linear absorption. For carrier densities  $N < 10^{28} \text{ m}^{-3}$ , well above densities created in our experiments, the change in dielectric constant is [40]

$$\Delta\epsilon_{\text{fc}} = - \left( \frac{\omega_P}{\omega} \right)^2 \left( 1 - i(\omega\tau_D)^{-1} \right), \quad (4)$$

where  $\omega_P^2 = Ne^2/(m^*\epsilon_0)$  is the plasma frequency squared in  $(\text{rad/s})^2$  and  $e$  and  $m^*$  are the charge and effective optical mass of the carriers, and  $\omega$  the probe frequency in  $\text{rad/s}$ . Equation 4 is valid for  $(\omega\tau_D)^{-1} \ll 1$ , which is the case for our probe frequencies and damping times. For a given  $I_{\text{Pump}}$  therefore, we can fit the differential reflectivity resulting from a changing  $\beta_{11}$  to  $(\Delta R/R)_{\text{FC}}$ .

The  $\beta_{11}$  versus  $E_{\text{Pump}}$  as returned from the fits is plotted in figure 6. For  $E_{\text{Pump}} < \frac{1}{2}E_G$ ,  $\beta_{11}$  tends to 0, as expected. Increasing  $E_{\text{Pump}}$  to above 0.54 eV, there is a marked increase. At  $E_{\text{Pump}} = 0.62 \text{ eV}$ ,  $\beta_{11}$  has increased to as much as  $5 \pm 1 \text{ cmGW}^{-1}$ . This value compares favorably to other values of p-Si samples: values as high as  $\beta_{11} = 60 \pm 15 \text{ cmGW}^{-1}$  have been reported [22]. Indeed, a systematic study by Ikeda *et al.* showed the nonlinear coefficient increases with increasing amorphousness of the sample, with  $\beta_{11} = 4 \text{ cmGW}^{-1}$  for p-Si samples, and up to  $120 \text{ cmGW}^{-1}$  for amorphous silicon [41]. To summarize this comparison, we plot our extracted values of  $\beta_{11}$  along with  $\beta_{11}$  of both p-Si and c-Si sample in fig. 6.

We are now able to calculate crucial parameters to characterize the quality of the switching process in terms of absorption and homogeneity. We find that the carrier induced absorption

length is  $\ell_{\text{abs}} = 123 \pm 50 \text{ } \mu\text{m}$ , much longer than the Bragg length  $L_B$ , confirming that the absorption is negligible indeed. The pump homogeneity length that describes the spatial homogeneity of carriers is  $\ell_{\text{hom}} = (I_{\text{Pump}}\beta_{11})^{-1} = 44 \pm 10 \text{ } \mu\text{m}$ , or  $170 \pm 40 L_B$  at  $E_{\text{Pump}} = 0.62 \text{ eV}$  and  $I_{\text{Pump}} = 46 \pm 5 \text{ GWcm}^{-2}$ . This calculation highlights the advantage of two-photon absorption [30] to one-photon absorption in which absorption strongly limits the pump homogeneity [17,18,42]. We conclude that for our switching conditions, both the pump and the probe absorption length remain well above  $L$ , and that thus instantaneous switching yields favorable conditions for our pump and probe frequencies, and pump intensities.

## 6. Interpretation of switched reflectivity at one probe frequency

Having analyzed spectra of the reflectivity at coincidence and at  $\Delta t = 1 \text{ ps}$ , we return to figure 3. Experimental conditions had prevented us from taking more than 4 probe frequency- and time-resolved spectra, mostly related to the long measurement times. Having identified two competing processes at coincidence, we can now focus on time-resolved spectra which depend on pump frequency only. Figure 7 shows  $(\Delta R/R)_{\text{coinc}}$  as a function of  $E_{\text{Pump}}$ . Here,  $I_{\text{Pump}}$  has been corrected for three important pump beam parameters: i., the increase in intensity with increasing  $E_{\text{Pump}}$  because of the decreasing Gaussian focus [43]; ii. the change in pump intensity due to the frequency dependent reflectivity of the pump, see figure 2; and iii. the measured 10% change in pump power over the frequency range of the OPA. For i.,  $(\Delta R/R)_{\text{coinc}}$  is taken to vary quadratically with  $E_{\text{Pump}}$ , assuming that  $(\Delta R/R)_{\text{coinc}}$  changes linearly with  $I_{\text{Pump}}$ . For ii,  $(\Delta R/R)_{\text{coinc}}$  was linearly corrected by a factor  $(1 - R(E_{\text{Pump}}))$ , where  $R_{\text{Pump}}(E_{\text{Pump}})$  is the reflectivity of the pump at the pump frequency. Finally, in iii., we corrected  $(\Delta R/R)_{\text{coinc}}$  linearly with  $I_{\text{Pump}}$ . The two largest corrections are by 80% ( $E_{\text{Pump}} = 0.52 \text{ eV}$ ) and 34% ( $E_{\text{Pump}} = 0.56 \text{ eV}$ ), but otherwise the corrections are less than 20%.

In figure 7 we observe an increasing negative differential reflectivity  $-(\Delta R/R)_{\text{coinc}}$  with increasing  $E_{\text{Pump}}$  up to 0.62 eV, then a decrease until 0.69 eV before a subsequent increase. With the analysis of the previous data (fig. 5), two important regimes can now be identified:

for  $E_{\text{Pump}} < 0.69$  eV ( $E_{\text{Total}} < 1.82$  eV),  $(\Delta R/R)_{\text{coinc}}$  is mostly governed by dispersion. For  $E_{\text{Pump}} > 0.69$  eV,  $(\Delta R/R)_{\text{coinc}}$  increases again due to a combination of both dispersive ( $n_2$ ) as well as absorptive parts ( $\beta_{12}$ ).

In figure 7 we also show the differential reflectivity expected from the extended SWA. Because this different reflectivity spectrum was obtained on domain A1, we first have to apply the SWA to the linear reflectivity from A1 (not shown). We obtain best agreement for  $G = 2\pi/(363 \text{ nm})$  and  $U_G = -1.2$ . From the theoretical relation for a degenerate  $n_2$  of a direct bandgap semiconductor [39],  $(\Delta R/R)_{\text{coinc}}$  is readily obtained. Since a nondegenerate theory for indirect bandgap semiconductors is not yet available, the theory has to be interpreted cautiously with respect to the measurement. For  $E_{\text{Pump}} < 0.7$  eV, the shape of the theoretical relation agrees excellently to our measurements. A strong divergence from the data is found for  $E_{\text{Pump}} > 0.7$  eV, or  $E_{\text{Total}} > 1.83$  eV. We interpret this threshold frequency as marking a transition from dispersive behavior of  $(\Delta R/R)_{\text{coinc}}$  to absorptive behavior.

To verify the consistency of the time- and frequency resolved  $(\Delta R/R)_{\text{coinc}}$  taken on domain D4 (see section 5.A) with the pump frequency resolved  $(\Delta R/R)_{\text{coinc}}$  taken on domain A1, both  $n_2$  and  $\beta_{12}$  (figure 5) were inserted into the SWA at A1, and plotted in figure 7. The obtained differential reflectivity is lower by a factor 2. Reasonable agreement to the measured differential reflectivity is found, from which we conclude that the extended SWA provides consistent description of our various data, measured at different pump intensities and on different sample domains.

## 7. Nondegenerate figure of merit for fs switching

To quantify how useable a material is for optical switching, it is vital to consider a figure of merit (FOM). A high FOM then is tantamount to a large phase shift, desirable for switching applications. Previously, Garmire proposed a degenerate FOM, a measure which indicates the maximum achievable phase shift of  $2\pi \times \text{FOM}$ , given that the device length is equal to the pump homogeneity length [44]. The absolute length of the device then depends on the

intensity used. From this requirement it follows that,

$$\text{FOM}(E_{\text{Pump}}) = \frac{n_2(E_{\text{Pump}})}{\lambda_{\text{Pump}}\beta_{11}(E_{\text{Pump}})}, \quad (5)$$

where  $\lambda_{\text{Pump}}$  is the pump wavelength. Here we extend this notion to the general case by including nondegenerate absorption: Not only is the pump absorbed because it excites free carriers, but the probe is absorbed in the presence of the pump. The nondegenerate FOM (NFOM) is then [45]

$$\text{NFOM}(E_{\text{Pump}}, E_{\text{Probe}}) = \frac{n_2(E_{\text{Pump}})}{\lambda_{\text{Pump}}\beta_{11}(E_{\text{Pump}}) + \lambda_{\text{Probe}}\beta_{12}(E_{\text{Pump}}, E_{\text{Probe}})}. \quad (6)$$

Because of the much lower probe intensity, we can neglect  $n_2(E_{\text{Probe}})$  in the numerator and  $\beta_{11}(E_{\text{Probe}})$  in the denominator. The NFOM has been calculated from our measured data as follows:  $n_2(E_{\text{Pump}})$  has been derived from figure 5(b), where we have used the functional form of  $n_2(E_{\text{Pump}})$  from [39], scaled by a constant factor to match the magnitude of our data. An analytic form of  $\beta_{12}$  was derived by fitting an exponential to the linear absorption coefficient  $\alpha(E_{\text{Pump}} + E_{\text{Probe}})$ . The exponential behavior of the F absorption coefficient  $\alpha$  with  $E_{\text{Probe}}$  close to the gap region is well documented [46]. From  $\alpha(E_{\text{Pump}} + E_{\text{Probe}})$ , we deduce  $\beta_{12} = \alpha(E_{\text{Pump}} + E_{\text{Probe}})/(2I_{\text{Pump}})$  from equation 7. Finally, an analytic expression for  $\beta_{11}(E_{\text{Pump}})$  is obtained from the theoretical relation for  $\beta_{11}(E_{\text{Pump}})$  for direct bandgap semiconductors from [39], scaled by a factor to match our measurements (fig. 6).

Figure 8 shows the NFOM for different  $E_{\text{Pump}}$  and  $E_{\text{Probe}}$ . At total frequencies  $E_{\text{Total}} = E_{\text{Pump}} + E_{\text{Probe}}$  below the optical gap of p-Si ( $E_{\text{Total}} < E_{\text{Opt}} \approx 1.5$  eV), the nondegenerate two-photon absorption is small, tantamount to a long probe absorption length, which is desired. If in addition  $E_{\text{Pump}} < \frac{1}{2}E_G$ , the pump absorption length becomes infinite. Higher order photon absorption has to be considered to quantitatively estimate the NFOM in this region of parameter space [47]. Around  $E_{\text{Pump}} = 0.8$  eV,  $n_2$  changes sign and thus the NFOM approaches 0. For all other frequencies, NFOM depends strongly on both pump

and probe frequencies. To achieve a high NFOM, it is best for  $E_{\text{Total}}$  to remain below the optical gap, while  $E_{\text{Pump}}$  should remain just below  $\frac{1}{2}E_G$ . In that case,  $n_2$  is high, while both  $\beta_{11}$  and  $\beta_{12}$  are kept low. We have indicated this line of maximum NFOM in fig. 8. These experimental conditions were recently realized by us on a GaAs/AlAs microcavity [48]. Our present measurements have taken place in the parameter space indicated by the box. In this region, we find NFOM between  $6 \times 10^{-4}$  for  $E_{\text{Probe}} = 1.24$  eV and  $E_{\text{Pump}} = 0.75$  eV, and NFOM = 0.05 for  $E_{\text{Probe}} = 1.09$  eV and  $E_{\text{Probe}} = 0.58$  eV. The only other measurement of  $n_2$  on a Si based photonic structure is from Ref. [16]. We conclude that for a judicious choice of pump and probe frequency, the NFOM can be maximized by limiting both pump and nondegenerate probe absorption.

## 8. Conclusion and recommendations

Using nondegenerate tunable pump-probe spectroscopy on a Si woodpile photonic band gap crystal, we have for the first time identified Kerr switching in photonic crystals. For pump+probe frequencies greater than the optical gap of p-Si, we additionally observe absorptive features, which we identify with nondegenerate two photon absorption. Using a heuristic model, we estimate the maximum change in the real part of the refractive index to be  $\Delta n' = 1.1 \times 10^{-3}$ , giving a Kerr coefficient of  $n_2 = 17 \times 10^{-6}$ , which is in good agreement to values in literature. The maximum imaginary part is  $1.1 \times 10^{-2}$ , corresponding to  $\beta_{12} = 1.19 \text{ cmGW}^{-1}$  at  $E_{\text{Pump}} = 0.62$  eV. This complex refractive index gives rise to reflectivity changes of 1%. From the interplay of these two effects we derive a nondegenerate figure of merit for instantaneous switching (NFOM). For a total pump+probe frequency in excess of the optical gap of Si, the NFOM is low, while opportune switching is achieved for low probe frequencies, and for  $E_{\text{Pump}} \sim 1/2E_G$ .

At probe delays of  $\Delta t = 1$  ps, we find that both pump and probe absorption is negligible, in agreement with a Drude description of the free carriers. The differential reflectivity spectra is purely dispersionlike, giving changes in reflectivity of up to  $\Delta R = 2.5\%$ . From this value we

deduce the maximum two-photon absorption coefficient to be  $\beta_{11} = 5 \text{ cmGW}^{-1}$ , in agreement to values stated in literature for p-Si.

In spite of the challenges in analyzing nondegenerate optical properties of a photonic band gap crystal, we have measured a clear difference in response of  $E_{\text{Total}} < E_{\text{Opt}}$  and  $E_{\text{Total}} > E_{\text{Opt}}$ . This difference has ramifications on future experiments on nondegenerate instantaneous switching photonic bandgap crystals. DOS switching, and ultimately spontaneous emission switching is limited by the magnitude of pump and emission frequencies.

To exploit Kerr switching, that is to maximize NFOM, following improvements are proposed. In first instance it seems useful to pump and probe with the same polarization. For collinear polarization, a factor 3 improvement is predicted with respect to orthogonal polarization [49]. Furthermore, the optical properties of the photonic crystal could be tailored so as to enhance the field. Calculations by us on a 1D Distributed Bragg Reflector have revealed that the field can significantly be enhanced when pumping at either the red or blue stopband edge, while the position of the field maximum depends critically on the exact pump frequency.

While a high-bandgap semiconductor will be less prone to nondegenerate absorption,  $n_2$  scales with  $E_G^{-3}$ , thus reducing the NFOM. The absorption can also be diminished by a lower pump intensity, which also goes at the expense of  $\Delta n'$ . We therefore conclude that judicious choice of semiconductor material, and pump and probe frequencies are required to usefully exploit Kerr switching.

## 9. Acknowledgements

We thank Henry van Driel and Allard Mosk for discussions, and Albert Polman for making the samples available. This work is part of the research program of the "Stichting voor Fundamenteel Onderzoek der Materie (FOM)", which was supported by the "Nederlandse Organisatie voor Wetenschappelijk Onderzoek (NWO)".



## References

1. P. M. Johnson, A. F. Koenderink, and W. L. Vos, “Ultrafast switching of photonic density of states in photonic crystals,” *Phys. Rev. B.* **66**, 081102(R) (2002).
2. B. P. J. Bret, T. L. Sonnemans, and T. W. Hijmans, “Capturing a light pulse in a short high-finesse cavity,” *Phys. Rev. A* **68**, 023807 (2003).
3. V. R. Almeida, C. A. Barrios, R. R. Panepucci, and M. Lipson, “All-optical control of light on a silicon chip,” *Nature* **431**, 1081 – 1084 (2004).
4. Q. Xu, V. R. Almeida, and M. Lipson, “Micrometer-scale all-optical wavelength converter on silicon,” *Opt. Lett.* **30**, 2733–2735 (2005).
5. S. F. Preble, Q. Xu, and M. Lipson, “Changing the colour of light in a silicon resonator,” *Nat. Phot.* **1**, 293–296 (2007).
6. P. J. Harding, T. G. Euser, Y. R. Nowicki-Bringuier, J.-M. Gérard, and W. L. Vos, “Ultrafast optical switching of planar GaAs/AlAs photonic microcavities,” *Appl. Phys. Lett.* **91**, 111103 (2007).
7. S. W. Leonard, H. M. van Driel, J. Schilling, and R. B. Wehrspohn, “Ultrafast band-edge tuning of a two-dimensional silicon photonic crystal via free-carrier injection,” *Phys. Rev. B.* **66**, 161102(R) (2002).
8. C. Becker, S. Linden, G. von Freymann, M. Wegener, N. Tétreault, E. Vekris, V. Kitaev, and G. A. Ozin, “Two-color pump-probe experiments on silicon inverse opals,” *Appl. Phys. Lett.* **87**, 091111 (2005).
9. T. G. Euser, H. Wei, J. Kalkman, Y. Jun, A. Polman, D. J. Norris, and W. L. Vos, “Ultrafast optical switching of three-dimensional Si inverse opal photonic band gap crystals,” *J. Appl. Phys.* **102**, 053111 (2007).
10. A. Chin, K. Y. Lee, B. C. Lin, and S. Horng, “Picosecond photoresponse of carriers in Si ion-implanted Si,” *Appl. Phys. Lett.* **69**, 653655 (1996).
11. M. Först, J. Niehusmann, T. Plötzing, J. Bolten, T. Wahlbrink, C. Moormann, and H. Kurz, “High-speed all-optical switching in ion-implanted silicon-on-insulator micror-

- ing resonators,” *Opt. Lett.* **32**, 2046–2048 (2007).
12. T. Tanabe, K. Nishiguchi, A. Shinya, E. Kuramochi, H. Inokawa, and M. Notomi, “Fast all-optical switching using ion-implanted silicon photonic crystal nanocavities,” *Appl. Phys. Lett.* **90**, 031115 (2007).
  13. M. Dinu, F. Quochi, and H. Garcia, “Third-order nonlinearities in silicon at telecom wavelengths,” *Appl. Phys. Lett.* **82**, 2954–2956 (2003).
  14. A. D. Bristow, N. Rotenberg, and H. M. van Driel, “Two-photon absorption and Kerr coefficients of silicon for 850 – 2200 nm,” *Appl. Phys. Lett.* **90**, 191104 (2007).
  15. Q. Lin, J. Zhang, G. Piredda, R. W. Boyd, P. M. Fauchet, and G. P. Agrawal, “Dispersion of silicon nonlinearities in the near infrared region,” *Appl. Phys. Lett.* **91**, 021111 (2007).
  16. A. Haché and M. Bourgeois, “Ultrafast all-optical switching in a silicon-based photonic crystal,” *Appl. Phys. Lett.* **77**, 4089–4091 (2000).
  17. D. A. Mazurenko, R. Kerst, J. I. Dijkhuis, A. V. Akimov, V. G. Golubev, D. A. Kurdyukov, A. B. Pevtsov, and A. V. Sel’kin, “Ultrafast optical switching in three-dimensional photonic crystals,” *Phys. Rev. Lett.* **91**, 213903 (2003).
  18. S. R. Hastings, M. J. A. de Dood, H. Kim, W. Marshall, H. S. Eisenberg, and D. Bouwmeester, “Ultrafast optical response of a high-reflectivity GaAs/AlAs Bragg mirror,” *Appl. Phys. Lett.* **86**, 031109 (2005).
  19. J. P. Mondia, H. W. Tan, S. Linden, H. M. van Driel, and J. F. Young, “Ultrafast tuning of two-dimensional planar photonic-crystal waveguides via free-carrier injection and the optical Kerr effect,” *J. Opt. Soc. Am. B.* **22**, 2480 (2005).
  20. Indeed, this Kerr nonlinearity was also claimed by our group [50], but was later corrected [21].
  21. T. G. Euser, A. J. Molenaar, J. G. Fleming, B. Gralak, A. Polman, and W. L. Vos, “All-optical octave-broad ultrafast switching of Si woodpile photonic band gap crystals,” *Phys. Rev. B* **77**, 115214 (2008).
  22. T. G. Euser, “Ultrafast optical switching of photonic crystals,” Ph.D. thesis, University

- of Twente, ISBN 978-90-365-2471-1, [www.photonicbandgaps.com](http://www.photonicbandgaps.com) (2007).
23. J. G. Fleming and S. Lin, “Three-dimensional photonic crystal with a stop band from 1.35 to 1.95 $\mu\text{m}$ ,” *Opt. Lett.* **24**, 49–51 (1999).
  24. K. M. Ho, C. T. Chan, and C. M. Soukoulis, “Existence of a photonic gap in periodic dielectric structures,” *Phys. Rev. Lett.* **65**, 3152–3155 (1990).
  25. B. Gralak, M. J. A. de Dood, G. Tayeb, S. Enoch, and D. Maystre, “Theoretical study of photonic band gaps in woodpile crystals,” *Phys. Rev. E* **67**, 066601 (2003).
  26. K. M. Ho, C. T. Chan, C. M. Soukoulis, R. Biswas, and M. Sigalas, “Photonic band gaps in three dimensions: New layer-by-layer periodic structures,” *Sol. St. Commun.* **89**, 413–416 (1994).
  27. W. L. Vos, H. M. van Driel, M. Megens, A. F. Koenderink, and A. Imhof, *Experimental probes of the optical properties of photonic crystals*, Proceedings of the NATO ASI ”Photonic Crystals and Light Localization in the 21st century” (Kluwer, Dordrecht, 2001). Edited by C. M. Soukoulis.
  28. A. F. Koenderink, “Emission and transport of light in photonic crystals,” Ph.D. thesis, University of Amsterdam, ISBN 90-9016903-2, [www.photonicbandgaps.com](http://www.photonicbandgaps.com) (2003).
  29. M. J. A. de Dood, B. Gralak, A. Polman, and J. G. Fleming, “Superstructure and finite-size effects in a Si photonic woodpile crystal,” *Phys. Rev. B* **67**, 035322 (2003).
  30. T. G. Euser and W. L. Vos, “Spatial homogeneity of optically switched semiconductor photonic crystals and of bulk semiconductors,” *J. Appl. Phys.* **97**, 043102 (2005).
  31. J. F. Reintjes and J. C. McGroddy, “Indirect two-photon transitions in Si at 1.06  $\mu\text{m}$ ,” *Phys. Rev. Lett.* **30**, 901–903 (1973).
  32. H. K. Tsang, C. S. Wong, T. K. Liang, I. E. Day, S. W. Roberts, A. Harpin, J. Drake, and M. Asghari, “Optical dispersion, two-photon absorption and self-phase modulation in silicon waveguides at 1.5  $\mu\text{m}$  wavelength,” *Appl. Phys. Lett.* **80**, 416–418 (2002).
  33. K. W.-K. Shung and Y. C. Tsai, “Surface effects and band measurements in photonic crystals,” *Phys. Rev. B* **48**, 11265–11269 (1993).

34. M. Deubel, M. Wegener, S. Linden, and G. von Freymann, “Angle-resolved transmission spectroscopy of three-dimensional photonic crystals fabricated by direct laser writing,” *Appl. Phys. Lett.* **87**, 221104 (2005).
35. J. A. Woollam Co., Inc., *Variable Angle Spectroscopic Ellipsometry Handbook (WVASE32)* (1987).
36. C. Rotaru, S. Nastase, and N. Tomozeiu, “Amorphous phase influence on the optical bandgap of polysilicon,” *Phys. Stat. Sol. (a)* **171**, 365–370 (1999).
37. H. Garcia and R. Kalyanaraman, “Phonon-assisted two-photon absorption in the presence of a dc-field: the nonlinear Franz-Keldysh effect in indirect gap semiconductors,” *J. Phys. B* **39**, 2737–2746 (2006).
38. Higher *probe* intensities do not influence the magnitude of the nondegenerate absorption: in the absence of linear absorption, as in our case, the differential equation governing nondegenerate two photon absorption is [51]

$$\frac{dI_{\text{Probe}}}{dz} = -2\beta_{12}(E_{\text{Probe}}, E_{\text{Pump}})I_{\text{Pump}}I_{\text{Probe}}(z). \quad (7)$$

Here,  $\beta_{12}$  is the nondegenerate two-photon absorption coefficient. From equation 7 we see that higher probe intensities do not increase absorption: The coefficient of  $-I_{\text{Probe}}(z)$  is  $2\beta_{12}(E_{\text{Probe}} + E_{\text{Pump}})I_{\text{Pump}} = \alpha_{\text{eff}}$ , which is an effective absorption coefficient. Higher probe intensities merely lead to a higher *absorbance*, commensurate to the number of absorbed photons.

39. M. Sheik-Bahae, D. J. Hagan, and E. W. Van Stryland, “Dispersion and band-gap scaling of the electronic Kerr effect in solids associated with two-photon absorption,” *Phys. Rev. Lett.* **65**, 96–99 (1990).
40. K. Sokolowski-Tinten and D. von der Linde, “Generation of dense electron-hole plasmas in silicon,” *Phys. Rev. B* **61**, 2643–2650 (2000).
41. K. Ikeda, Y. Shen, and Y. Fainman, “Enhanced optical nonlinearity in amorphous silicon

- and its application to waveguide devices,” *Opt. Expr.* **15**, 17761–17771 (2007).
42. I. Fushman, E. Waks, D. Englund, N. Stoltz, P. Petroff, and J. Vučković, “Ultrafast nonlinear optical tuning of photonic crystal cavities,” *Appl. Phys. Lett.* **90**, 091118 (2007).
  43. We had independently measured the radius of the beam waist at the focus, and had confirmed that the radius is diffraction limited.
  44. E. Garmire, “Nonlinear optics in semiconductors,” *Phys. Today* **47**, 42–48 (1994).
  45. We note that the  $n_2$  in equation 6 depends on  $E_{\text{Pump}}$  only. Measurements of nondegenerate  $n_2$  are still lacking in literature.
  46. C. Klingshirn, *Semiconductor Optics* (Springer, 2005).
  47. S. Pearl, N. Rotenberg, and H. M. van Driel, “Three photon absorption in silicon for 2300 – 3300 nm,” *Appl. Phys. Lett.* **93**, 131102 (2008).
  48. A. Hartsuiker, P. J. Harding, Y.-R. Nowicki-Bringuier, J.-M. Gérard, and W. L. Vos, “Kerr and free-carrier ultrafast all-optical switching of GaAs/AlAs nanostructures near the three-photon edge of GaAs,” *J. Appl. Phys.* **104**, 083105 (2008).
  49. M. Sheik-Bahae, J. Wang, and E. W. Van Stryland, “Nondegenerate optical Kerr effect in semiconductors,” *IEEE J. Quant. Elect.* **30**, 249–255 (1994).
  50. T. G. Euser, A. J. Molenaar, J. G. Fleming, B. Gralak, A. Polman, and W. L. Vos, “All-optical ultrafast switching of Si woodpile photonic band gap crystals,” *arXiv:physics p. 0603045v1* (2006).
  51. D. C. Hutchins and E. W. Van Stryland, “Nondegenerate two-photon absorption in zinc blende semiconductors,” *J. Opt. Soc. Am. B.* **9**, 2065–2074 (1992).
  52. P. Paddon and J. F. Young, “Two-dimensional vector-coupled-mode theory for textured planar waveguides,” *Phys. Rev. B* **61**, 2090–2101 (2000).

## List of Figure Captions

Fig. 1 High resolution scanning electron micrograph of the surface normal to [001] of a Si woodpile crystal at domain D4. The width and thickness of each rod is  $175 \pm 10\text{nm}$  and  $155 \pm 10\text{nm}$ , respectively.

Fig. 2 Linear reflectivity spectrum of the woodpile photonic crystal measured normal to the [001] direction at a sample domain D4 shown in figure 1. The E-field is perpendicular to the first row of rods. A stopgap near 0.9 eV gives rise to a high maximum reflectivity of  $95 \pm 2\%$  and has a broad relative width of 47%, indicating a high photonic strength. At high frequencies  $> 1.2$  eV, the spectral features are attributed to Fabry-Pérot-type fringes. The pump frequencies (shaded box) were tuned at the red edge through half the electronic band gap  $E_G = 1.12$  eV of silicon (vertical dashed line), and the probe frequencies at the blue edge of the stopband. The dashed curve is a calculation with the Scalar Wave Approximation in the region of interest.

Fig. 3 Differential reflectivity  $\Delta R/R$  versus probe delay  $\Delta t$  taken at different pump frequencies  $E_{\text{Pump}}$  and at probe frequency  $E_{\text{Probe}} = 1.13$  eV, sample domain A1. At  $\Delta t = 0$  ps, the pump and probe are coincident, and the differential reflectivity  $(\Delta R/R)_{\text{coinc}}$  decreases. At  $\Delta t = 1$  ps, the differential reflectivity  $(\Delta R/R)_{\text{FC}}$  has increased due to the dispersion of the free carriers (FC). The peak pump intensity varies between  $I_{\text{Pump}} = 10 \pm 1 \text{ GWcm}^{-2}$  ( $E_{\text{Pump}} = 0.516$  eV) and  $I_{\text{Pump}} = 25 \pm 2 \text{ GWcm}^{-2}$  ( $E_{\text{Pump}} = 0.75$  eV), and the probe intensity was  $I_{\text{Probe}} = 3 \pm 2 \text{ GWcm}^{-2}$ .

Fig. 4 (a): Measured linear reflectivity versus probe frequency (open squares) on domain D4 compared to the scalar wave approximation (solid curve). (b) The differential reflectivity  $(\Delta R/R)_{\text{FC}}$  at delay  $\Delta t = 1$  ps caused by the free carriers shows mostly dispersive features, as seen from the symmetric variation of  $\Delta R/R$  around 0. When increasing the pump frequency from 0.54 (solid triangles) to 0.62 eV (open triangles), these dispersive features increase in magnitude. (c): At  $\Delta t = 0$  ps, dispersive as well as absorptive features are observed in  $(\Delta R/R)_{\text{coinc}}$ , increasingly so when increasing the pump frequency from  $E_{\text{Pump}} = 0.54$  eV to

0.62 eV. For  $E_{\text{Pump}} = 0.54$  eV, we find  $\Delta n' = 0.44 \times 10^{-3}$  and  $n'' = 0.46 \times 10^{-3}$ , while for  $E_{\text{Pump}} = 0.62$  eV the fits give  $\Delta n' = 1.1 \times 10^{-3}$  and  $n'' = 1.1 \times 10^{-2}$ . The pump intensity was  $I_{\text{Pump}} = 36 \pm 4 \text{ GWcm}^{-2}$  ( $E_{\text{Pump}} = 0.54$  eV) and  $I_{\text{Pump}} = 46 \pm 5 \text{ GWcm}^{-2}$  ( $E_{\text{Pump}} = 0.62$  eV).

Fig. 5 Instantaneous changes of the complex refractive index. (a): Imaginary refractive index ( $n''$ , solid squares) vs. pump frequency  $E_{\text{Pump}}$  (lower axis) obtained from fits in fig. 4. The dashed curve is a fit of  $n''$  to an exponential. The right scale shows the corresponding absorption coefficient. For comparison, we plot the absorption coefficient for low pressure chemical vapor deposited p-Si (solid curve) annealed at 545°C, similar to the backbone of our woodpile crystals. Upper abscissa is the sum of the pump and probe frequencies  $E_{\text{Total}}$ . (b): Change in real refractive index  $\Delta n'$  (left scale, solid squares) vs. pump frequency  $E_{\text{Pump}}$  from our nondegenerate measurements. The theoretical relation predicted by [39] is also shown (solid curve, right scale). We plot degenerate measurements for comparison: Open squares from [13] and open circles from [15]. Data from [14] exceeds the scale by one order of magnitude.

Fig. 6 Nonlinear coefficient  $\beta_{11}$  vs. pump frequency (solid squares) obtained from data as in fig. 4. Dashed curve is a calculation from Ref. [39] for c-Si. Other data are from [13] (c-Si, open squares), [15] (c-Si, open circles), [14] (c-Si, triangles) and [41] (p-Si, diamonds).

Fig. 7 Differential reflectivity at coincidence vs. pump frequency extracted from figure 3 (domain A1) and corrected for pump beam parameters (squares, left scale). Circles are complex values of  $n$  extracted from fig. 5 (domain D4) and reinserted in the extended SWA at domain A1. We have calculated the differential reflectivity expected from a nonlinear, purely dispersive direct bandgap material (solid curve) [39] by inserting the theoretical relation for  $n_2$  into the extended SWA. The 'purely dispersive assumption' deviates from the data for pump frequencies above  $E_{\text{Pump}} = 0.69$  eV, or  $E_{\text{Total}} = 1.82$  eV.

Fig. 8 Nondegenerate Figure of Merit (NFOM) for instantaneous switching vs. pump and probe frequency for polysilicon (see eq. 6). For  $E_{\text{Pump}} < \frac{1}{2}E_G$  ( $=0.56$  eV), pump absorption

is absent as we do not consider more than second order photon absorption. If in addition  $E_{\text{Pump}} + E_{\text{Probe}} < E_{\text{Opt}} = 1.5 \text{ eV}$ , the total absorption is 0 leading to large NFOM outside of the scale of graph (crossed area). The black curve indicates the parameter space for which a maximum NFOM is reached if three photon absorption is neglected. At  $E_{\text{Pump}} = 0.8 \text{ eV}$ ,  $n_2(E_{\text{Pump}})$  crosses  $0 \text{ cm}^2\text{GW}^{-1}$ , and so the NFOM vanishes. For  $E_{\text{Total}} \gg E_{\text{Opt}}$ , the NFOM is  $< 1 \times 10^{-5}$  (hatched area). The parameter space in our present measurements are bounded by the box (squares). The only other measurement of  $n_2$  on a Si based photonic structure is [16] (circle).

Fig. 9 (a) Relative change in frequency  $\Delta E/E_0$  for a given change in the relative average refractive index  $\Delta n_{\text{av}}/n_{\text{av}}$ . For comparison, the change according to Bragg's law  $\Delta E/E_0 = -\Delta n_{\text{av}}/n_{\text{av}}$ . (b) Change in reflectivity for a given change in imaginary part of the refractive index  $n''$ . C

Fig. 10 Reflectivity calculated with the scalar wave approximation, with and without the thin layer of SiN.



### A. Comparison of the scalar wave approximation to the exact modal method

To assess whether the changes in spectral properties resulting from a change in  $n'$  and  $n''$  agree with the induced changes in the EMM, we compare the spectral changes for a given  $n'$  or  $n''$ . Figure 9(a) shows the relative change in frequency for a given change in average refractive index. The shift  $\Delta E$  due to  $\Delta n'$  at the same probe frequency is compared. We find that for changes  $\Delta n' < 0.2$ , which is more than two orders of magnitude larger than our expected  $\Delta n' = 1 \times 10^{-3}$ , the agreement is even better than 5%. The good agreement for both  $\Delta n'$  and  $\Delta n''$  proves indeed that the two requirements are sufficient for the description of the dynamic reflectivity. Therefore, spectral properties associated with the vectorial nature of the probe, such as TE-TM mixing [52] or polarization effects [29], have a negligible effect on the *change* in reflectivity. In figure 9(b) we show the expected change in reflectivity for a given change in  $n''$ . To include absorption in the SWA, the reflectivity is reduced by  $\exp(-2L/\ell_{\text{abs}})$ , where  $\ell_{\text{abs}} = \lambda_0/(4\pi n''\phi)$ . The factor of 2 in the exponent accounts for the beam passing through the sample twice. For  $E_{\text{Probe}} = 1.19$  eV, and for  $\Delta n'' < 0.1$ , which is around 10 times larger than expected, the agreement is better than 5%.

From the good agreement between the exact modal method (EMM) and the extended scalar wave approximation, we conclude that the heuristic accurately predicts the change in complex refractive index.

### B. Effect of SiN on linear reflectivity spectrum

In order to verify that the layer of SiN supporting the woodpile has negligible effect on the linear reflectivity, a calculation of the SWA is performed with this layer. Figure 10 shows the reflectivity spectra, without and with the supporting SiN layer (70 nm). The spectra shifts by 6.2 meV at the most in our region of interest. Therefore we conclude that the inclusion of this layer has only a negligible effect on the linear spectra.

## Figures

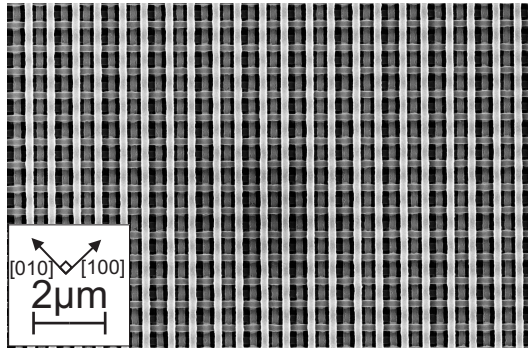


Fig. 1. High resolution scanning electron micrograph of the surface normal to  $[001]$  of a Si woodpile crystal at domain D4. The width and thickness of each rod is  $175 \pm 10\text{nm}$  and  $155 \pm 10\text{nm}$ , respectively. SEMD4.eps

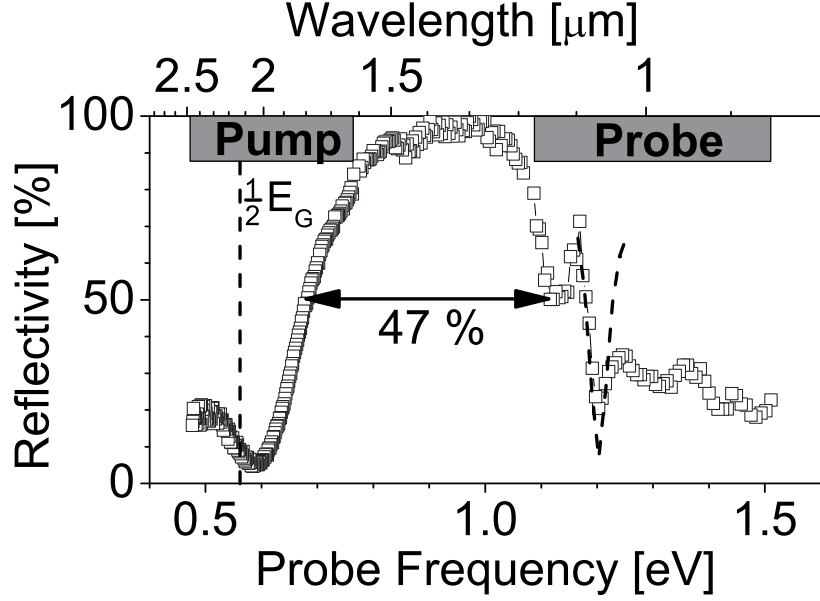


Fig. 2. Linear reflectivity spectrum of the woodpile photonic crystal measured normal to the  $[001]$  direction at a sample domain D4 shown in figure 1. The E-field is perpendicular to the first row of rods. A stopgap near 0.9 eV gives rise to a high maximum reflectivity of  $95 \pm 2\%$  and has a broad relative width of 47%, indicating a high photonic strength. At high frequencies  $> 1.2$  eV, the spectral features are attributed to Fabry-Pérot-type fringes. The pump frequencies (shaded box) were tuned at the red edge through half the electronic band gap  $E_G = 1.12$  eV of silicon (vertical dashed line), and the probe frequencies at the blue edge of the stopband. The dashed curve is a calculation with the Scalar Wave Approximation in the region of interest. ReflExtAllD4.eps

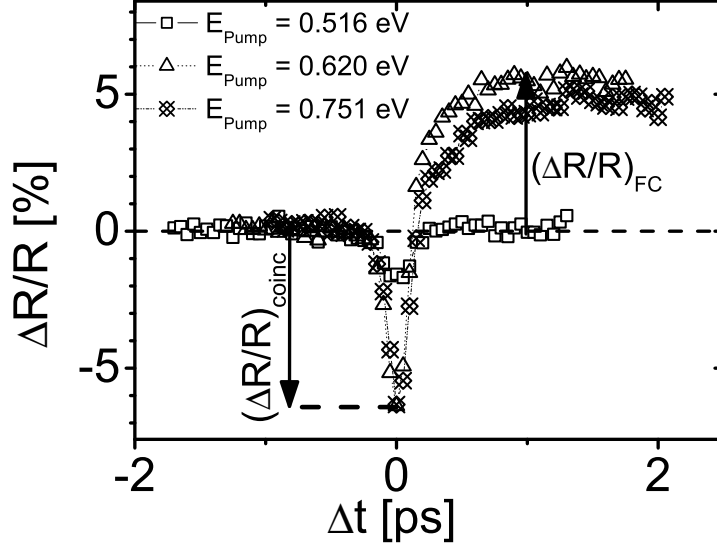


Fig. 3. Differential reflectivity  $\Delta R/R$  versus probe delay  $\Delta t$  taken at different pump frequencies  $E_{\text{Pump}}$  and at probe frequency  $E_{\text{Probe}} = 1.13$  eV, sample domain A1. At  $\Delta t = 0$  ps, the pump and probe are coincident, and the differential reflectivity  $(\Delta R/R)_{\text{coinc}}$  decreases. At  $\Delta t = 1$  ps, the differential reflectivity  $(\Delta R/R)_{\text{FC}}$  has increased due to the dispersion of the free carriers (FC). The peak pump intensity varies between  $I_{\text{Pump}} = 10 \pm 1 \text{ GWcm}^{-2}$  ( $E_{\text{Pump}} = 0.516$  eV) and  $I_{\text{Pump}} = 25 \pm 2 \text{ GWcm}^{-2}$  ( $E_{\text{Pump}} = 0.75$  eV), and the probe intensity was  $I_{\text{Probe}} = 3 \pm 2 \text{ GWcm}^{-2}$ . DiffdRRvst.eps

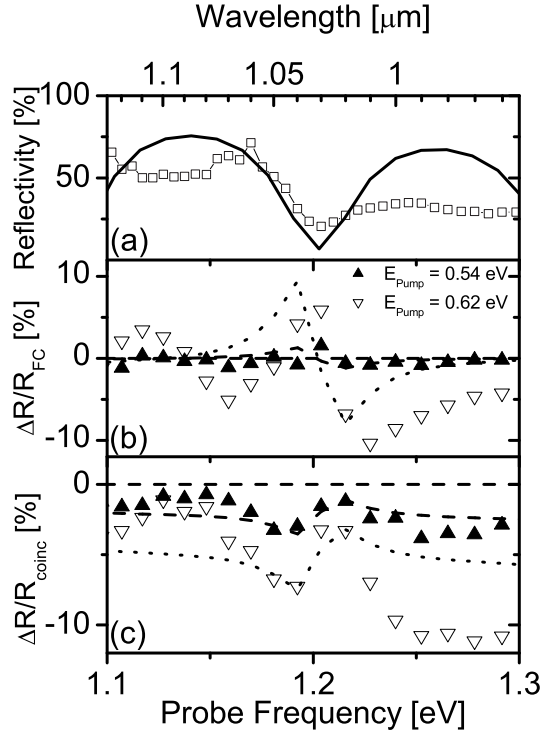


Fig. 4. (a): Measured linear reflectivity versus probe frequency (open squares) on domain D4 compared to the scalar wave approximation (solid curve). (b) The differential reflectivity  $(\Delta R/R)_{\text{FC}}$  at delay  $\Delta t = 1$  ps caused by the free carriers shows mostly dispersive features, as seen from the symmetric variation of  $\Delta R/R$  around 0. When increasing the pump frequency from 0.54 (solid triangles) to 0.62 eV (open triangles), these dispersive features increase in magnitude. (c): At  $\Delta t = 0$  ps, dispersive as well as absorptive features are observed in  $(\Delta R/R)_{\text{coinc}}$ , increasingly so when increasing the pump frequency from  $E_{\text{Pump}} = 0.54$  eV to 0.62 eV. For  $E_{\text{Pump}} = 0.54$  eV, we find  $\Delta n' = 0.44 \times 10^{-3}$  and  $n'' = 0.46 \times 10^{-3}$ , while for  $E_{\text{Pump}} = 0.62$  eV the fits give  $\Delta n' = 1.1 \times 10^{-3}$  and  $n'' = 1.1 \times 10^{-2}$ . The pump intensity was  $I_{\text{Pump}} = 36 \pm 4$   $\text{GWcm}^{-2}$  ( $E_{\text{Pump}} = 0.54$  eV) and  $I_{\text{Pump}} = 46 \pm 5$   $\text{GWcm}^{-2}$  ( $E_{\text{Pump}} = 0.62$  eV).

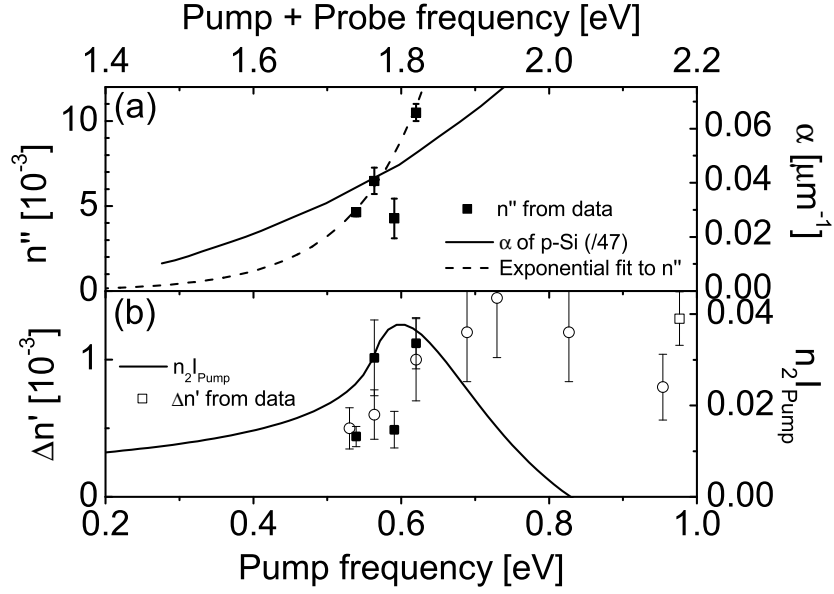


Fig. 5. Instantaneous changes of the complex refractive index. (a): Imaginary refractive index ( $n''$ , solid squares) vs. pump frequency  $E_{\text{Pump}}$  (lower axis) obtained from fits in fig. 4. The dashed curve is a fit of  $n''$  to an exponential. The right scale shows the corresponding absorption coefficient. For comparison, we plot the absorption coefficient for low pressure chemical vapor deposited p-Si (solid curve) annealed at 545°C, similar to the backbone of our wood-pile crystals. Upper abscissa is the sum of the pump and probe frequencies  $E_{\text{Total}}$ . (b): Change in real refractive index  $\Delta n'$  (left scale, solid squares) vs. pump frequency  $E_{\text{Pump}}$  from our nondegenerate measurements. The theoretical relation predicted by [39] is also shown (solid curve, right scale). We plot degenerate measurements for comparison: Open squares from [13] and open circles from [15]. Data from [14] exceeds the scale by one order of magnitude.

ExtractCmplxn.eps

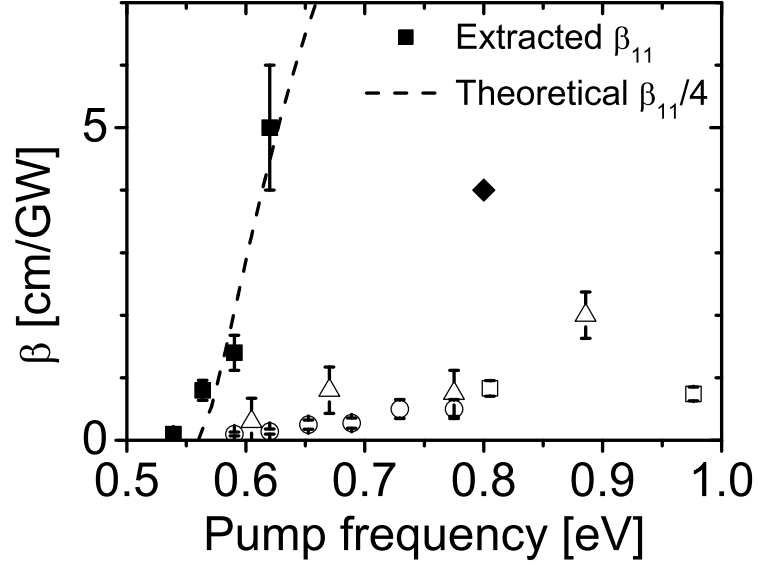


Fig. 6. Nonlinear coefficient  $\beta_{11}$  vs. pump frequency (solid squares) obtained from data as in fig. 4. Dashed curve is a calculation from Ref. [39] for c-Si. Other data are from [13] (c-Si, open squares), [15] (c-Si, open circles), [14] (c-Si, triangles) and [41] (p-Si, diamonds). beta.eps

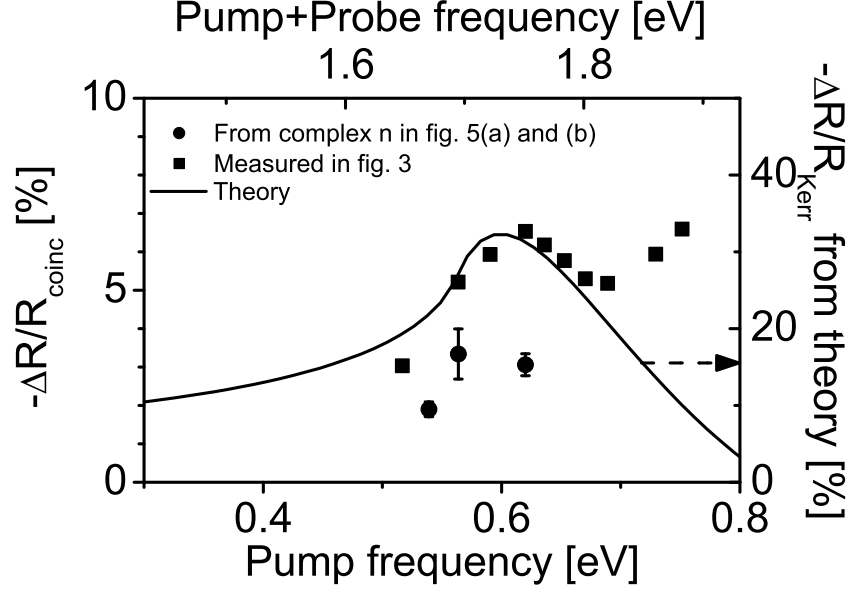


Fig. 7. Differential reflectivity at coincidence vs. pump frequency extracted from figure 3 (domain A1) and corrected for pump beam parameters (squares, left scale). Circles are complex values of  $n$  extracted from fig. 5 (domain D4) and reinserted in the extended SWA at domain A1. We have calculated the differential reflectivity expected from a nonlinear, purely dispersive direct bandgap material (solid curve) [39] by inserting the theoretical relation for  $n_2$  into the extended SWA. The 'purely dispersive assumption' deviates from the data for pump frequencies above  $E_{\text{Pump}} = 0.69$  eV, or  $E_{\text{Total}} = 1.82$  eV.

KerrScaledwTheory.eps



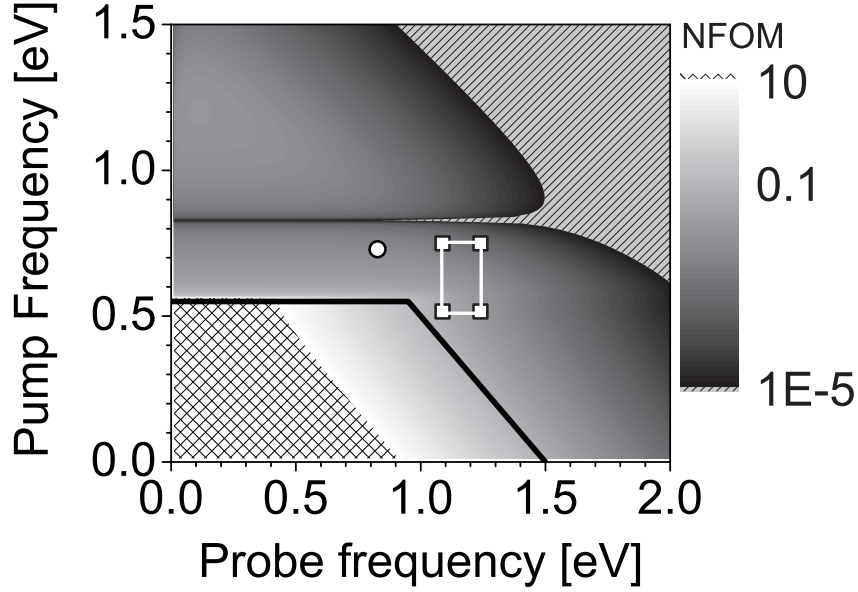


Fig. 8. Nondegenerate Figure of Merit (NFOM) for instantaneous switching vs. pump and probe frequency for polysilicon (see eq. 6). For  $E_{\text{Pump}} < \frac{1}{2}E_G$  ( $=0.56$  eV), pump absorption is absent as we do not consider more than second order photon absorption. If in addition  $E_{\text{Pump}} + E_{\text{Probe}} < E_{\text{Opt}} = 1.5$  eV, the total absorption is 0 leading to large NFOM outside of the scale of graph (crossed area). The black curve indicates the parameter space for which a maximum NFOM is reached if three photon absorption is neglected. At  $E_{\text{Pump}} = 0.8$  eV,  $n_2(E_{\text{Pump}})$  crosses  $0 \text{ cm}^2\text{GW}^{-1}$ , and so the NFOM vanishes. For  $E_{\text{Total}} \gg E_{\text{Opt}}$ , the NFOM is  $< 1 \times 10^{-5}$  (hatched area). The parameter space in our present measurements are bounded by the box (squares). The only other measurement of  $n_2$  on a Si based photonic structure is [16] (circle).

NFOM.eps

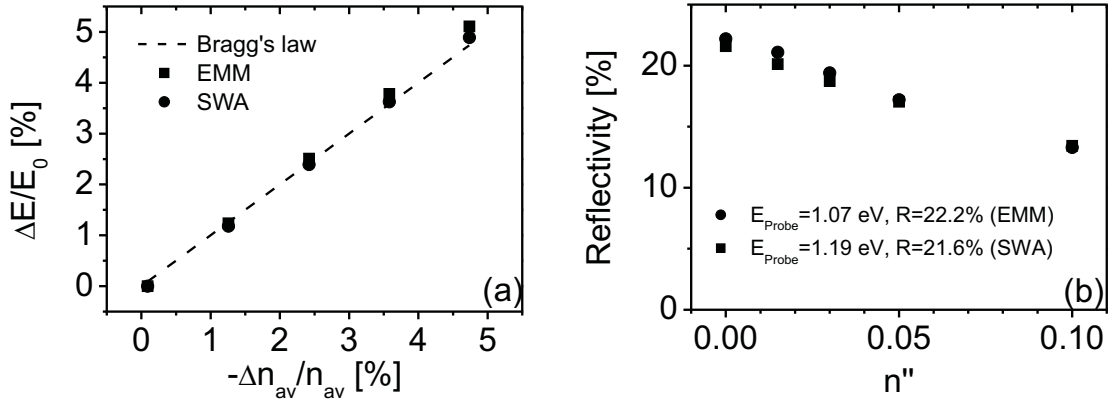


Fig. 9. (a) Relative change in frequency  $\Delta E/E_0$  for a given change in the relative average refractive index  $\Delta n_{av}/n_{av}$ . For comparison, the change according to Bragg's law  $\Delta E/E_0 = -\Delta n_{av}/n_{av}$ . (b) Change in reflectivity for a given change in imaginary part of the refractive index  $n''$ . CmpEMMSWA.eps

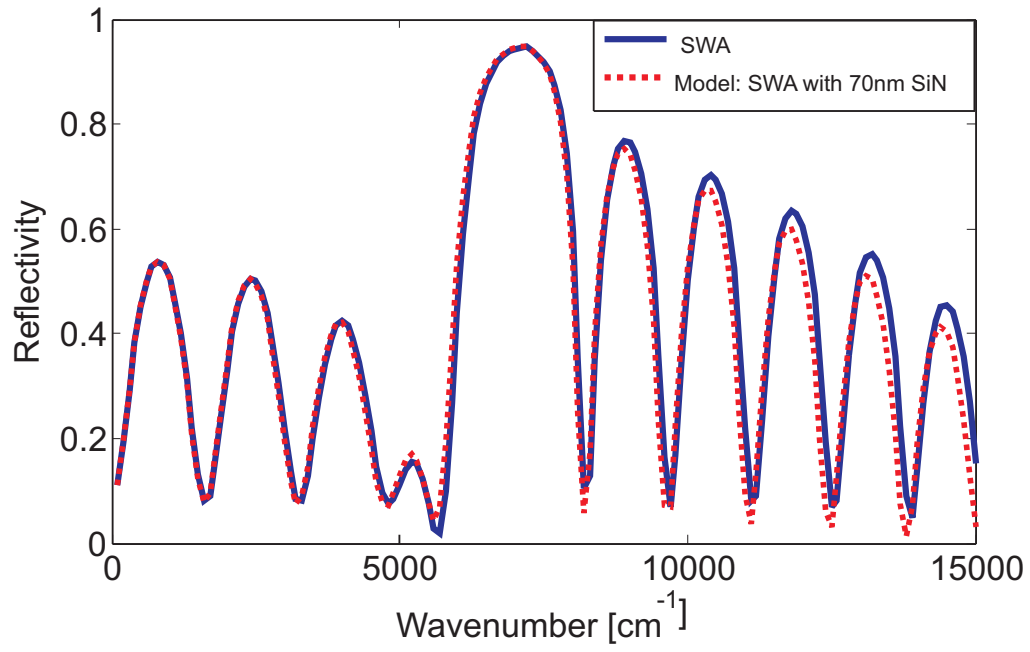


Fig. 10. Reflectivity calculated with the scalar wave approximation, with and without the thin layer of SiN. CmpSiNnoSiN.eps